A Geometric Method for Automatic Extraction of Sulcal Fundi

Chiu-Yen Kao, Michael Hofer, Guillermo Sapiro *Senior Member, IEEE*, Josh Stern, Kelly Rehm,
and David A. Rottenberg

Abstract—Sulcal fundi are 3D curves that lie in the depths of the cerebral cortex and, in addition to their intrinsic value in brain research, are often used as landmarks for downstream computations in brain imaging. In this work we present a geometric algorithm that automatically extracts the sulcal fundi from magnetic resonance images and represents them as spline curves lying on the extracted triangular mesh representing the cortical surface. The input to our algorithm is a triangular mesh representation of an extracted cortical surface as computed by one of several available software packages for performing automated and semi-automated cortical surface extraction. Given this input we first compute a geometric depth measure for each triangle on the cortical surface mesh, and based on this information we extract sulcal regions by checking for connected regions exceeding a depth threshold. We then identify endpoints of each region and delineate the fundus by thinning the connected region while keeping the endpoints fixed. The curves thus defined are regularized using weighted splines on the surface mesh to yield high-quality representations of the sulcal fundi. We present the geometric framework and validate it with real data from human brains. Comparisons with expert-labeled sulcal fundi are part of this validation process.

Index Terms—Brain imaging, MRI, sulcal fundi, brain warping, surface splines, thinning.

I. INTRODUCTION

WHEN viewed from the outside, a human brain appears as a volume with a highly wrinkled boundary surface having numerous long furrows. The term *sulci* (plural of *sulcus*) is associated with these furrows and the term *gyri* (plural of *gyrus*) designates the regions between the sulci. *Fundus* (literally meaning bottom) is applied to sulci to describe the deepest part of each furrow when viewed in cross section. The Neuroanatomist's concept of sulcal fundus is also constrained by the idea that a given sulcus's fundus is a continuous 1D curve (branching if and only if its sulcus branches) connecting all the sulcus's endpoints. There are a variety of ways in which the Neuroanatomist's intuitive, definitions of sulcus, sulcal fundus, and sulcal endpoint can be made geometrically

precise — i.e., by describing exactly which parts of a brain surface are to be considered sulcus and which 1D curve lying within each sulci is to be considered its fundus. This paper introduces an improved system of definitions along with efficient computational algorithms for realizing these definitions, and validates the performance of these algorithms using landmark data provided by Neuroanatomists.

Beyond the possible intrinsic relevance of sulcal research [1], [2], the importance of curvilinear representations of sulcal fundi lies in their use as landmarks for constraining (and thereby improving the identification of) deformation fields in both surface-based (e.g. [3], [4]) and volumetric (e.g. [5], [6]) brain warping algorithms. Sulcal depth assignments can also be used by surface warping algorithms that depend on optimizing the alignment of dense "iconic" features sets — e.g. [7]. Surface-to-surface brain warping has been used for longitudinal and cross-sectional studies of, e.g., brain structure and function, cortical thickness, and gray-matter density, c.f. [8] and the references therein.

Traditionally cortical sulci and sulcal fundi have been manually defined by labeling voxels in an MRI brain volume using a GUI which displays three orthogonal 2D brain slices. This process is extremely tedious, time consuming and notoriously prone to error (e.g., due to the fact that the sulcal troughs curve in three dimensions simultaneously, and the normal direction corresponding to "depth" can change rapidly as the surface undulates). Furthermore, manually labeled fundi in the volume data have to be projected onto the extracted surface for use as landmarks in surface based brain warping algorithms, and this process may lead to unanticipated results (i.e. naively projecting each point individually to the nearest surface location may lead to multiple unconnected and self-intersecting curves on the surface). Automating sulcal fundi extraction can ultimately improve the quality and reproducibility of the process as well as yielding considerable time savings.

A. Problem Statement and Contributions

A fully automated method for the extraction of sulcal fundi from MRI brain volumes combines an automated method for extracting a 3D, polyhedral mesh representation of a cortical brain surface with an automated method for defining fundal curves that lie on the mesh surface (or equivalently, parametric/implicit surfaces). In this paper, we do not introduce a new approach to cortical surface extraction; rather, we describe a method for defining sulcal depth and sulcal fundi given
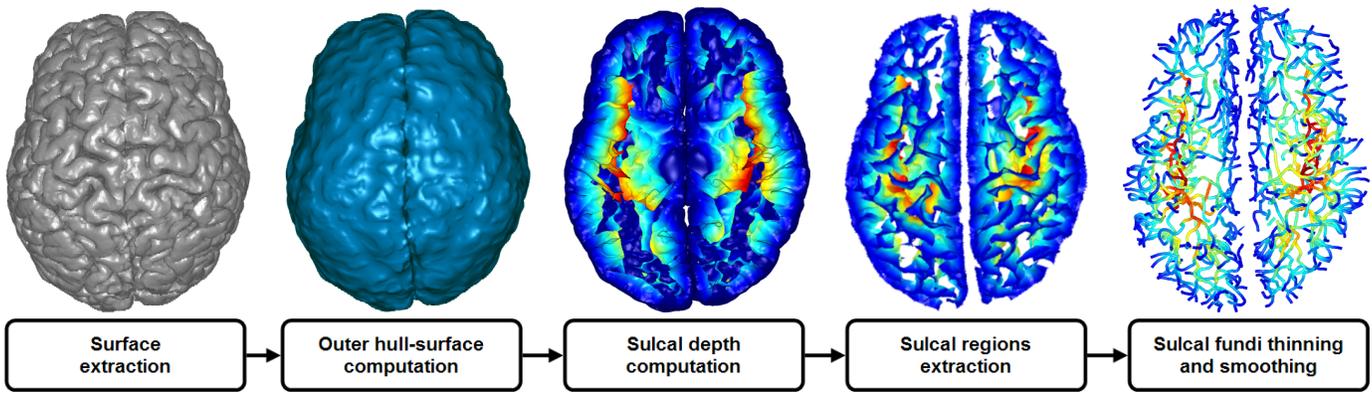
Fig. 1. Overview of the main steps of our algorithm. (All figures of the paper are in color.)

a closed mesh representation of the gray-matter (GM) and cerebrospinal fluid (CSF) boundary of a cortical hemisphere as an algorithmic input. There are a number of available software packages that can be utilized to generate such a mesh, including FreeSurfer[1] [9], SurfRelax[2] [10], and BrainVisa[3] [11]. Reference [12] provides an overview and discussion of methods that have been proposed to extract the cortical surface in implicit, parametric, or mesh representations. These methods have been primarily developed for cortical surface mesh extraction from "high resolution" (e.g., $1\ mm$ cubic voxels) T1-weighted brain images. We optimized the parameters in our experiments for normal human adult brains. However, by adjusting these parameters the same method can be employed for different types of brains (e.g., children, non-normal).

Improving the accuracy of surface extraction algorithms remains an active area of research in neuroimage analysis. For the validation work described here we chose to use data produced by FreeSurfer as our inputs, but the idea underlying our work is that the triangle mesh input has become a reasonably standard form of intermediate result in Neuroimaging. We believe our algorithm will work well with closed mesh surfaces produced by many other surface extraction packages; overall accuracy will be increased by future improvements in the surface extraction.

In this paper we present a geometric algorithm that aims at extracting the complete set of sulcal fundi as a network of partially connected curves that are guaranteed to be on the extracted brain surface. To validate our results we compare a subset of automatically extracted fundi to manually extracted ones as marked by expert anatomists in the volume image.

A flow chart illustrating the major steps of our algorithm is shown in Fig. 1. In the first step, the triangular mesh representing the cortical surface is extracted (this process actually consists of a number of sub-steps involving additional preprocessing algorithms prior to surface extraction proper, which are described in more detail below). Second, an outer hull surface which wraps the cortical surface is constructed. Third, numbers representing sulcal depth (measured in millimeters

according to minimal path-based distance between the input surface and the outer hull) are assigned to every point on the surface mesh. Fourth, based on the sulcal depth measure, the sulcal regions are extracted. Fifth and finally, the fundus curves obtained by thinning the sulcal regions are smoothed using weighted splines on the surface mesh to yield a high-quality curve representation. Each step of the algorithm is described in detail in Section II of the paper. Our key contributions are

- a novel depth measure that is anatomically reasonable,
- an automatic algorithm that aims at the extraction of a complete set of sulcal fundi, and
- a high-quality representation of the fundi as smooth curves lying on the pial (mesh input) surface.

The algorithmic steps outlined in Fig. 1 lead to a complete system for automatic extraction of fundi curves. In Sect. III we present experiments to validate our automatic results via comparison with curves traced by two experts. Furthermore, reproducibility studies are presented as well. In Sect. IV we discuss the relation of our work to prior art and in Sect. V we conclude the paper with an outlook towards future research.

II. METHODS

In this section we explain in detail the main steps of our algorithm, which can be sketched as follows. The input to our algorithm is a T1-weighted MRI human brain volume. For skull stripping, segmentation of the brain into white matter, gray matter, and cerebrospinal fluids, and for extraction of a triangle mesh surface from the MRI volume data, we use publicly available software. Then we use a regular grid to derive an implicit representation of the pial surface. Using a level set technique we compute an outer hull surface that encloses the pial surface in a shrink-wrap type fashion. The outer hull is such that one can still distinguish the gyri, but the sulcal regions are now covered. Then we define a novel depth measure for the pial surface as the shortest distance that connects each surface point to a point of the outer hull such that the point path stays inside the sulcal regions. The computational realization uses a fast sweeping algorithm. We are now able to extract the sulcal regions by thresholding the computed depth. We identify endpoints of the sulcal fundi and extract the fundi by a thinning algorithm. Such extracted curves are then smoothed using weighted splines in manifolds.
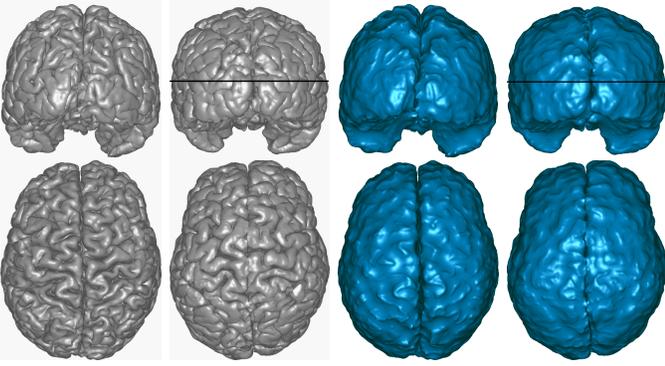
Fig. 2. Pial surfaces (left) and outer hulls (right) for different brains: Front and top view. The black lines mark where we cut the surfaces for the illustration in Fig. 5.

Fig. 3. Axial, coronal, and sagittal slices of the MRI brain volume and the outer hull surface of one hemisphere.

A. Segmentation, Surface Extraction, and Representation

A topologically correct triangular mesh representing the pial (GM/CSF) surface of the cerebral cortex was extracted by FreeSurfer[4] [9] after skull stripping using BET[5] [13]. In Fig. 2 we show front and top views of the extracted pial surfaces (using FreeSurfer) for different human brains.

By T_M we denote a triangle mesh with faces $T_1, \ldots, T_N$; we require T_M to be a closed and orientable 2-manifold in Euclidean 3-space. Our approach to the definition of sulcal depth is based on a level set technique. In order to apply it, the triangular-mesh representation is transformed into an implicit representation by computing the signed distance function to the surface on a Cartesian grid. In the implicit form, the pial surface becomes the zero level set $\{\Phi = 0\}$ of the signed distance function Φ. We obtain the signed distance function in two steps.

In the first step, the signed distance function Φ is efficiently computed (within machine accuracy [14], [15]) up to a given maximum distance d, i.e., in a band of width $2d$ extending from both sides of the surface. We choose $d = 5\ mm$ in our implementation. For each component (face, edge, and vertex) of the triangular-mesh, a polyhedron which contains its Voronoi cell as a subset is constructed. By using the scan conversion algorithm, one can determine which grid points are possibly within the given distance of the component and compute the distance. Since there are overlapping regions of polyhedra, some grid points may be scan converted more than once. In this case, the distance which has smaller magnitude is chosen.

In the second step, the eikonal equation

$$|\nabla \Phi(x, y, z)| = \sqrt{\Phi_x^2 + \Phi_y^2 + \Phi_z^2} = 1$$

is solved for the remaining grid points which have distances greater than $5\ mm$. This is done using a fast sweeping algorithm [16], [17], [18]. This gives the first order approximation of the distance function for the grid points away from the surface. We combine these two algorithms in order to maintain
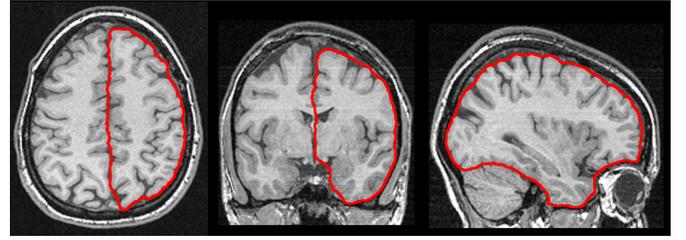
---

[4]*FreeSurfer*, see http://surfer.nmr.mgh.harvard.edu/
[5]*Brain Extraction Tool (BET)*, see http://www.fmrib.ox.ac.uk/fsl/bet/

high accuracy near the surface and efficiency for the overall distance computation.

Now for the pial surface we have both, an explicit triangular-mesh representation, and an implicit level-set representation on a Cartesian grid.

B. Outer Hull Surface Extraction

An outer hull surface, which wraps the pial surface is computed using a morphological closing operation applied to the level set function Φ [19]. Note that even the gross shape of the human cortex is far from being convex (see e.g. Fig. 2), so computing convex hulls after smoothing would not produce desirable results. For morphological closing we move the surface outward by a time parameter T and then move the surface inward by the same amount of time. The governing equation is

$$\left\{ \begin{array}{rcc} \Phi_t + V(t)|\nabla \Phi| & = & 0 \\ \Phi(x, y, z, 0) & = & \Phi(x, y, z), \end{array} \right.$$

where

$$V(t) = \left\{ \begin{array}{ccc} 1 & \text{for} & t \leq T \\ -1 & \text{for} & T < t \leq 2T \end{array} \right\}.$$

In our algorithm we choose $T = 10$ (mm/unit time). This is based on the width of sulcal regions. We want to choose the parameter T to be large enough to close the sulcal regions and small enough to maintain the overall shape of the brain. Practical experimentation has shown us that overall algorithm results are relatively insensitive to 50% increases or decreases in this parameter. The above equation is implemented with standard numerics.

The implicit representation of the outer hull surface is given by

$$\Psi(x) = \min \left\{ \Phi(x, y, z, 2T), \Phi(x, y, z, 0) \right\}.$$

The minimum in the formula enforces the condition that the outer hull surface wraps — but does not penetrate — the pial surface. We illustrate the computed outer hull surface for different brains in Fig. 2. In Fig. 3 we show an axial, coronal, and sagittal slice of the original MRI brain volume combined with the intersection curve of the outer hull surface in these slices.

C. Geodesic Depth Computation

After we obtain the outer hull surface, we calculate the geodesic depth (distance) for any given point on the pial
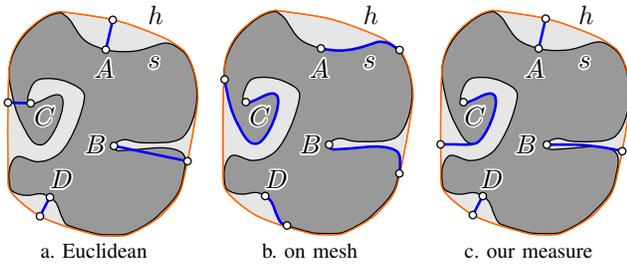
Fig. 4. A 2D illustration comparing the depth computation as explained in the text: (a) Euclidean, (b) on mesh, (c) our measure.
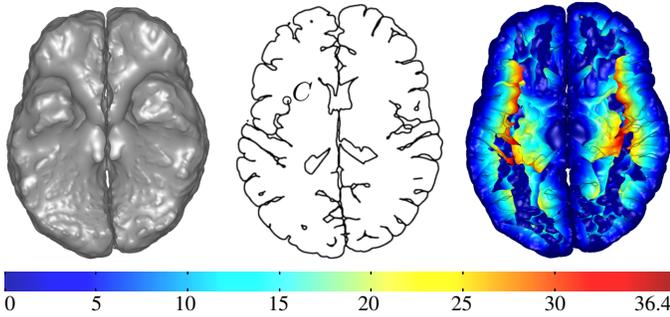

Fig. 5. We slice through the pial and hull surface at height indicated in Fig. 2 with a black line. (Left) The bottom half of the hull surface in top view. (Middle) The intersection curve with the pial surface. (Right) The bottom half of the pial surface in top view. The color corresponds to the computed depth from the hull. (Bottom) The color bar shows depth in mm.
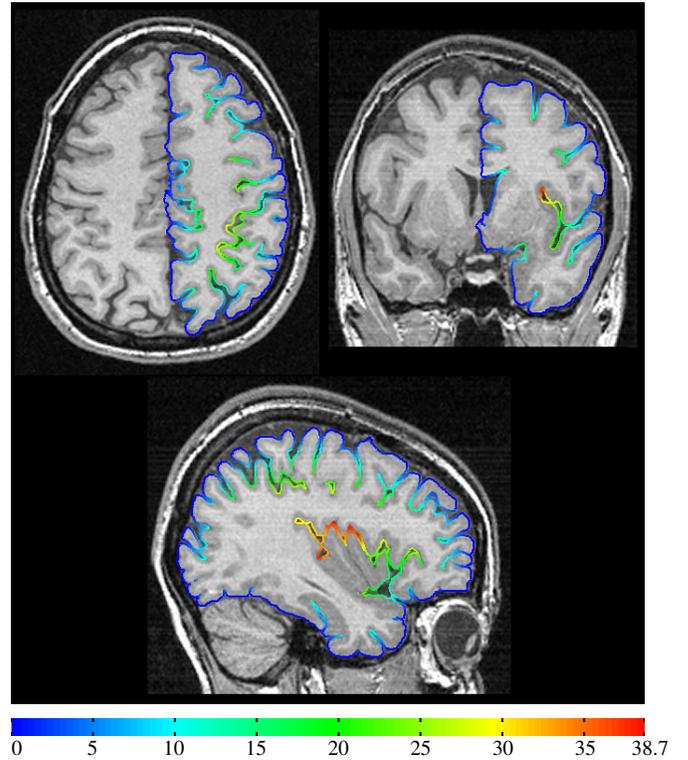

Fig. 6. Color coded geodesic depth (see color bar) displayed on axial, coronal, and sagittal slices of the pial surface overlaid onto the MRI brain volume.

surface to the outer hull. The desired geodesics correspond to the shortest paths from each pial surface location to the outer hull which do not cross the surface of the brain, i.e., the volume enclosed by the pial surface is considered as an obstacle that needs to be avoided by the paths. Our approach is different from that of previous work of [20] and [21], which either consider the Euclidean distance to the outer hull (Fig. 4a) or the geodesic distance on the triangular mesh (Fig. 4b). The depth measure we propose is illustrated in Fig. 4c. By the depth measure of [20] (Fig. 4a), point C and point D are approximately the same Euclidean distance from the hull curve h. By the depth measure of [21] (Fig. 4b), point A and point B are approximately the same geodesic distance to the hull h along the curve s. In our approach (Fig. 4c) the order of the depth is $d(C) > d(B) > d(A) \cong d(D)$, which is intuitively more correct. In all three illustrative drawings the thick blue curves illustrate the respective geodesic curves from the fundus points A, B, C, D to the outer hull h.

The geodesic depth calculation is done in three dimensions by applying the fast sweeping method [16], [17], [18] to the restricted (CSF) region between the outer hull and the pial surface $\{\Psi \leq 0 \text{ and } \Phi \geq 0\}$. The calculation is performed on a refined rectangular grid. Then, using trilinear interpolation, we propagate the depth information onto each triangle T_i of the triangular-mesh surface T_M. In Fig. 5 (right) we show in a top view the bottom part of the pial surface with the top part removed. The color coding corresponds to the computed geodesic depth, where blue indicates shallow and red indicates deep. The pial surface is cut open by the plane indicated in Fig. 2 as a black line, and Fig. 5 (middle) illustrates the

corresponding intersection curve. In Fig. 6 we display axial, coronal, and sagittal slices of a MRI brain volume onto which we overlay the color coded geodesic depth of the extracted pial surface.

D. Sulcal Fundus Extraction

The algorithmic steps described above result in the association of a sulcal depth estimate $d(T_i)$ with each mesh triangle T_i. Next, we use a depth threshold d_T to define the sulcal regions of the pial surface as those triangles with a depth $d(T_i) > d_T$, see Fig. 1 (second image from the right). In the literature [21], d_T is usually considered to be $2 - 3\ mm$. We use $d_T = 2.5\ mm$ (using an adaptive threshold is open to future refinements). Within these sulcal regions we find the connected components C_i by a connected components labeling algorithm [22]. For the remainder of the algorithm we only use those components that have more than a minimum number of triangles (see Section III for details).

For each component C_i we compute the strip B_i of boundary triangles. The next stage of our algorithm identifies a small subset of each B_i which constitutes the endpoints of the sulcus (a non-branching sulcus has exactly two endpoints; a branching sulcus is illustrated in Fig. 7). The algorithm for identifying endpoints uses the barycenters p_j of the triangles in the set B_i, and is based on the concept that the point set $\{p_j\}$ is of a curve-like nature with one or more endpoints. To identify these endpoints we associate with each point p_j of B_i a principal component direction of the set of points N_{p_j} in a local neighborhood around p_j, and we identify as endpoints those points p_j which are extremal according to the principal
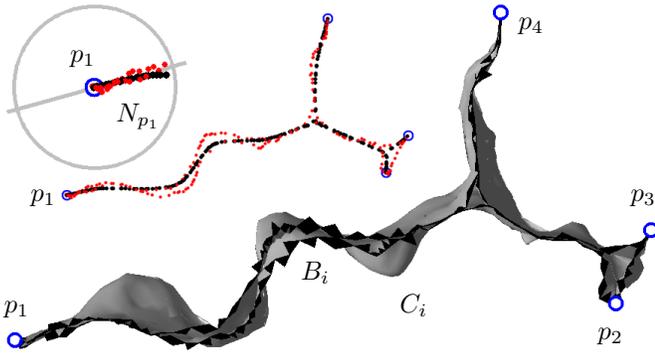
Fig. 7. Fundi endpoints $p_1, \ldots, p_4$ of a component C are those points of the boundary of the C that are extremal according to the principal component direction in a local neighborhood N_{p_j}.

Fig. 8. The longest non-branching path (illustrated as a thick 3D curve c) for the component shown in Fig. 7 runs from endpoint p_1 to endpoint p_2.

component direction in their local neighborhood N_{p_j}. We use a moving least squares (MLS) algorithm [23] to compute the local principal component directions. The example shown in Fig. 7 illustrates a component C_i with the set of boundary triangles B_i and the four endpoints $p_1, \ldots, p_4$ identified by our algorithm.

In the next step of our fundi extraction algorithm we run, for each component C_i, a surface thinning algorithm. We then take those triangles of the boundary strip B_i that correspond to the computed endpoints p_j and add them to an initial skeleton list S_i. The following two steps are then repeated until all triangles of the component C_i have been processed:

1) Find the triangle Δ of B_i with the least depth.
2) If removing Δ would change the connectivity of the mesh, then add Δ to the skeleton list S_i. Else, we remove Δ from the list of boundary triangles B_i and add the edge neighbor triangles of Δ to B_i.

The result of the thinning algorithm is the skeleton S_i of each connected component C_i, which is made up of connected strips of triangles. We then use a minimum spanning tree algorithm [24] to construct the tree structure of S_i. The longest non-branching path within the tree can be calculated by iteratively discarding the shortest branch leaving each vertex that has degree greater than two until only vertices of degree one and two remain. The thick 3D curve in Fig. 8 illustrates the longest non-branching path for the component shown in Fig. 7 (the other fundal branches for this component are not shown). By connecting the barycenters of the triangle strips we get our initial fundi curves. In Fig. 9 we show all automatically extracted fundi as thick 3D curves, where the color corresponds to the geodesic depth (blue is shallow, yellow is medium, and red is deep).

E. Sulcal Fundi Smoothing

The extracted sulcal fundi are so far only polygons connecting the barycenters of the extracted triangle strips. We smooth these polygons by an algorithm that minimizes a counterpart to the cubic spline energy for curves on surfaces. For that purpose we extend the algorithm of [25] to *weighted* spline
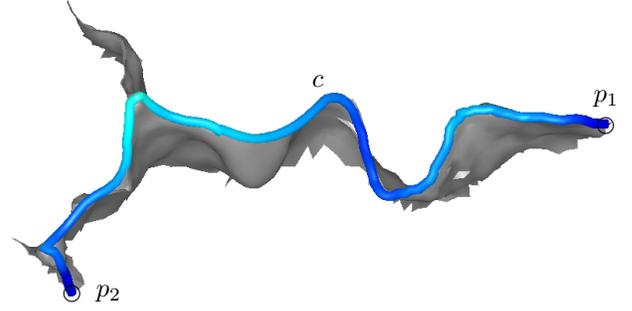
curves $c(u)$ in manifolds, minimizing the energy

$$E(c) = \int_{u_1}^{u_n} w(c(u)) \|\ddot{c}(u)\|^2 du, \qquad (1)$$

under the constraint that $c(u)$ is on a surface. If we want the curve to stay in the deep part of the sulcus, then we have to choose a small weight w for these regions. This is achieved by choosing the weight w as a function depending on the computed geodesic depth $d(c(u))$ at the curve point $c(u)$,

$$w(c(u)) := \frac{1}{1 + d(c(u))^\alpha}.$$

The weight so defined is locally smaller for the fundus area than for the remaining sulcal region with shallower geodesic depth. The basic idea of the smoothing algorithm involves interleaving the steps of numerically minimizing the energy of a weighted spline curve and projection of the curve to lie on the mesh surface. A detailed analysis for splines on manifolds (without weights) is given in [25]. Here we present the extension to weighted splines using a straightforward optimization procedure for minimizing (1) with a projected gradient descent algorithm.

We consider a polygon $p = (p_1, p_2, \ldots, p_K)$, which is an ordered sequence of K points $p_k \in \mathbb{R}^3$, as a discrete curve representing a sulcal fundi. Furthermore we have an associated sequence of weights $w = (w_1, \ldots, w_K)$. The weight $w_k := 1/(1 + d(p_k)^\alpha)$ belongs to the point p_k whose geodesic depth is $d(p_k)$ and we set $\alpha = 2$. In the present application, the polygon always has two endpoints and all polygon vertices are constrained to lie on the pial surface S. We want to minimize the discrete version of the energy (1) under the nonlinear side condition that the polygon p is constrained to S. The discrete energy $E(p)$ is given by

$$E(p) = \sum_{k=1}^{K} w_k \|\Delta^2 p_k\|^2, \qquad (2)$$

where the second difference vector is given by

$$\Delta^2 p_k := p_{k-1} - 2p_k + p_{k+1}, \quad (1 < k < K), \qquad (3)$$

and we set $\Delta^2 p_1 = \Delta^2 p_K = 0$. We collect all second difference vectors in a second difference polygon of length K,

$$\Delta^2 p := (\Delta^2 p_1, \Delta^2 p_2, \ldots, \Delta^2 p_K). \qquad (4)$$
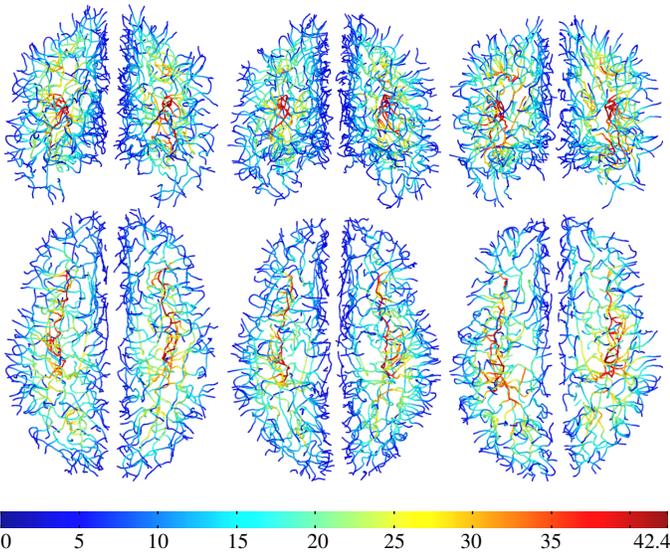
Fig. 9. All automatically extracted sulcal fundi illustrated as thick 3D curves for the brains of Fig. 2: Front and top view. The color visualizes geodesic depth in mm as indicated by the color bar. To better see all fundi curves we do not show the pial surface.
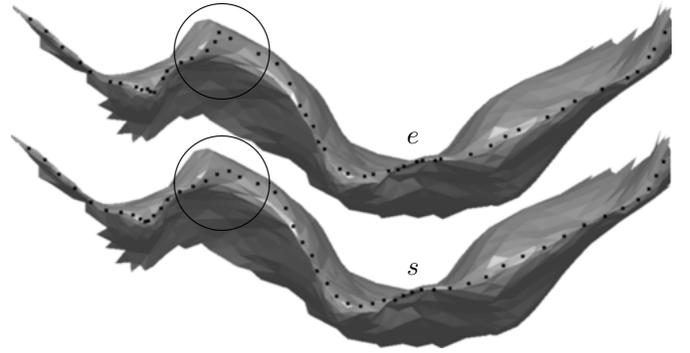

Fig. 10. Surface constrained sulcal fundi smoothing illustrated for typical fundi: Black dots indicate the points of the fundus polygon after extraction (e) and after smoothing (s). Note for example the regions inside the circles.

We define $q_k := w_k(p_{k-1} - 2p_k + p_{k+1})$ for $1 < k < K$. Using this notation the gradient $\nabla E(p)$ of the energy function $E(p)$ can be written as

$$\nabla E(p) = 2(q_2, -2q_2 + q_3, q_{k-1} - 2q_k + q_{k+1},$$
$$q_{K-2} - 2q_{K-1}, q_{K-1}), \qquad (5)$$

where $k = 3, \ldots, K - 3$. To compute the optimal stepsize s for the current descent direction $q = -\nabla E(p)$ we note that the energy function $E(p + sq)$ for p and q fixed is a quadratic function in s. Thus a simple calculation leads to the optimal choice of s,

$$s = -\langle diag(w)\Delta^2 q, \Delta^2 p \rangle / \langle diag(w)\Delta^2 q, \Delta^2 q \rangle,$$

where the second difference polygon $\Delta^2 p$ is defined in (4) and $\Delta^2 q$ is defined completely analogous; $\langle \cdot, \cdot \rangle$ denotes the standard scalar product in $\mathbb{R}^{3K}$ and $diag(w)$ is a block diagonal matrix whose non-zero entries are taken from the weight sequence w.

Geometrically we interpret the gradient $\nabla E(p)$ as a sequence of vectors $v_1, \ldots, v_K$ that are attached to the points $p_1, \ldots, p_K$ of our polygon. Since we want to minimize the energy of the polygon p under the nonlinear constraint that p lies on the surface S, we project the vectors v_k into the tangent spaces of S at p_k. Given two unit length basis vectors a_k, b_k of the tangent space at each point p_k, the projected vectors are $v_k^T := \langle a_k, v_k \rangle a_k + \langle b_k, v_k \rangle b_k$.

Now the polygon for the next iteration step is obtained by projecting the points $p_k + sv_k^T$ back onto the surface S. For those points that shall be kept fixed we simply set $v_k^T := 0$. In Fig. 10 we compare typical fundi polygons before and after smoothing. For better comparison we only show the vertices of the polygon.

III. EXPERIMENTS, DATA ANALYSIS AND EVALUATION

We evaluated the validity of our algorithm via comparison with sulcal fundi delineated by two expert raters ("the validity experiment") from six subjects, and tested the reproducibility of the algorithm by measuring the distance between sulcal fundi extracted from two separately acquired image volumes from the same subject ("the reproducibility experiment"). In both cases, we also quantify the fraction of the discrepancy that may be attributable to inaccuracies or variance in the extracted surface inputs to the fundus detection algorithm.

A. Image Data

Image data for the validity experiment consisted of MR volumes of six normal adult subjects acquired at the Montreal Neurological Institute and provided to us by Dr. Alan C. Evans. Image data for the reproducibility experiment, provided to us by Dr. Roger Woods, consisted of a pair of MR volumes from the same adult subject acquired in two different scanning sessions using two different MR pulse sequences (see [26] for further detail). All images were T1 weighted (1.5T) with spatial resolution of 1.0 mm^3. Triangular mesh surfaces as well as splines representing the fundi of all detected sulci were extracted by our automated algorithm for both cortical hemispheres of all eight image volumes. The same processing and parametric details described in Sect. II (Methods) were used in each case.

B. Validity Evaluation of Our Algorithm on Six Subjects

For the six brains that we used for validity evaluation, the extracted pial surfaces consist of an average number of 392455 triangles per hemisphere with a standard deviation of 10047. On average the area of the outer hull surface compromises 37.1% of the area of the pial surface (with a standard deviation of 0.0061%). The maximum geodesic depth of the sulcal regions assumes for the six brains a mean value of 38.36 mm with a standard deviation of 2.30 mm. By using a threshold of $d_T = 2.5$ mm the extracted sulcal regions (see Sect. II-D) compromise a mean 66.7% of the pial surface with a standard deviation of 0.008% (for 6 brains). The average geodesic depth of the sulcal regions for the six brains has a mean value of 11.73 mm with a standard deviation of 0.17 mm.

As mentioned in Sect. II-D, after extracting sulcal regions, we next find the connected components within those regions.
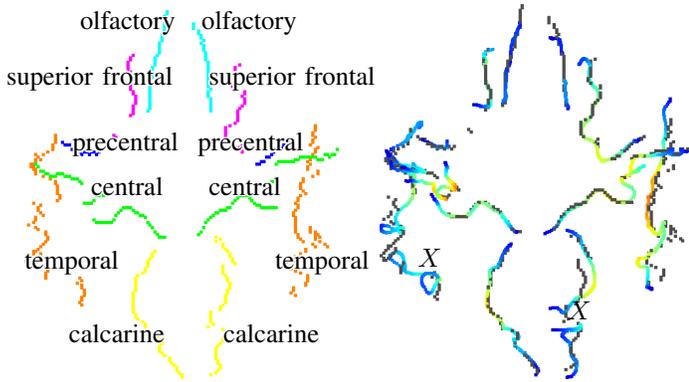
Fig. 11. (Left) The 6 sulcal fundi manually-labeled by an expert anatomist on each of the brain hemispheres for a single brain. (Right). The sulcal fundi automatically extracted by our algorithm closest to the manually marked voxels shown as black dots. The symbol X marks areas where the extracted pial surface obviously is incorrect.

Fig. 12. (Left) We compute the closest points p_s of manually-labeled voxels p_m on the pial surface S, and then measure the distance $r = \|p_s - p_a\|$ to the automatically extracted points p_a. (Right) The two images illustrate the cortical surface in relation to the brain parenchyma, a manually-labeled point p_m, and an automatically-labeled point p_a on the fundus of the left superior temporal sulcus.

The average number of sulcal region components per hemisphere (for $d_T = 2.5\ mm$) is 43.25 with a standard deviation of 3.54. However, several of these components only consist of a few triangles and are therefore not useful for further processing. We discard all components that have less than 50 triangles which leaves us with an average number of 33.5 (and a standard deviation of 4.03) components per hemisphere.

Note that the threshold d_T is not critical for our algorithm. By using a smaller value the fundi endpoints we find move closer to the outer hull. A larger threshold will move the fundi endpoints further inward and return more components per hemisphere. However, e.g., the olfactory sulcal fundi is rather shallow and will be missed if d_T is too large. It is interesting to note that the sulcal regions are highly connected:

- the largest component compromises an average 62% of the sulcal regions (with a standard deviation of 12%), and
- the largest five components compromise an average 86% of the sulcal regions (with a standard deviation of 5%).

Note that the number of components per se is not relevant for our algorithm. However, the small number of components that make up a large part of the human brain indicate the interconnectedness of the sulcal regions. Our sulcal fundi extraction algorithm preserves these connections. Our algorithm returns a rich set of automatically-extracted sulcal fundi which are illustrated in Fig. 9 in top and front view as thick 3D curves, where the color indicates the geodesic depth.

Remark. To use our automated extraction technique for applications where two endpoints for each fundal landmark are explicitly required, one could proceed as follows: After our large network of sulcal fundi has been extracted and smoothed on the pial surface, one could interactively mark the two endpoints of as many fundi curves as needed and then use the such chosen curves as landmarks for downstream applications in Computational Anatomy.

Two different expert raters manually marked voxel locations representing the fundi of the calcarine, central, olfactory,
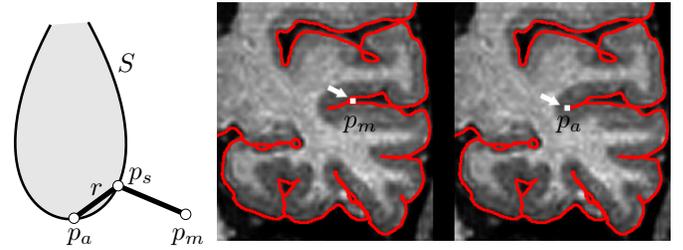
precentral, superior frontal and temporal sulci on both hemispheres (see Fig. 11, left) of the six volumes featured in the validity experiment. These six sulci were carefully chosen to satisfy the following criteria: 1) they are present in a recognizable, similar form in almost all adult subjects, 2) Neuroanatomists agree on their description and nomenclature, and 3) they are spread out over different parts of the brain. These attributes makes these sulci particularly suitable as landmarks relevant to intersubject brain registration.

The visualization and labeling software utilized by the raters allowed for simultaneous viewing of each image location in the three standard orthogonal viewing planes as well as standard image processing operations such as zoom and contrast enhancement.

The manual labeling is carried out in the MRI volume data. So the manually marked voxels are, in general, not lying on the extracted pial surface. For landmark-based surface warping, the manually marked fundi are usually projected onto the pial surface. Thus, for comparison of our automatic results to the hand-marked ones (see Fig. 11, right), it makes sense to also perform this projection. In the following we denote an automatically extracted fundus point by p_a, a manually marked fundus point by p_m, and the projection of p_m onto its closest point on the extracted pial surface by p_s, see Fig. 12 (left). Then we adopt, as a basic unit of error, the Euclidean distance $r = \|p_s - p_a\|$.

Since the set of manually marked sulcal fundi is not intended to be exhaustive in any sense, our basic notion of performance for this experiment is the extent to which for all manually labeled points p_m the error r is small. Aside from any potential shortcomings in our definition of sulcal depth and fundal location, there are several possible other reasons for geometric divergence. These reasons include errors in the underlying extracted mesh surface (see the symbol X in Fig. 13) and errors in the manual labeling (see the circled areas in Fig. 13).

In Figure 14 we illustrate the manual fundi labeling results with several consecutive slices of the MRI volume data for the central sulcus. Figure 15 displays the frequency histograms of the error $r = \|p_s - p_a\|$ for different brains and two different raters (experts). The histograms show that there are outliers with large values of r up to $12\ mm$, although the total number of such outliers is small. The numbers n_1, n_2 of manually-
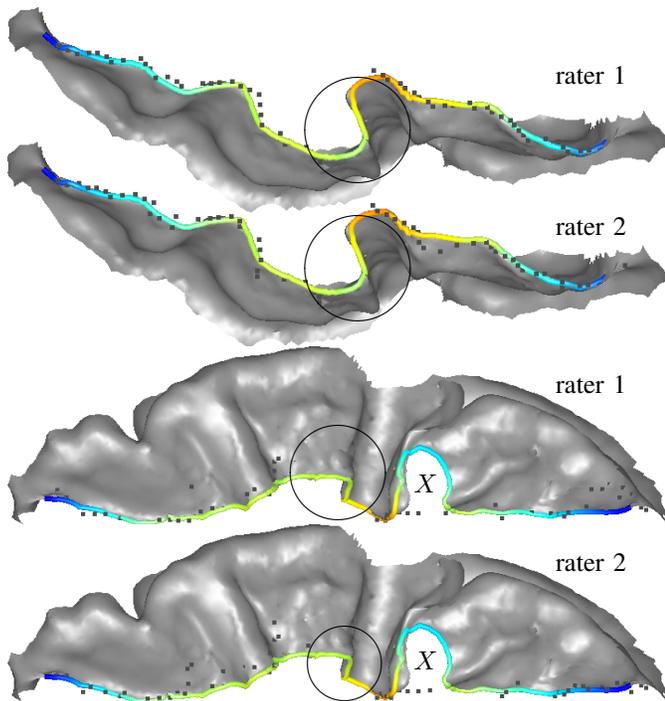
Fig. 13. Comparison of the automatically extracted fundi (thick curve) with the manually marked voxels (black dots) for two different central sulci. Note the different results of the two raters and that both miss the middle part marked by a circle (which happened in all six brains we looked at). The symbol X marks an error in the extracted pial surface.
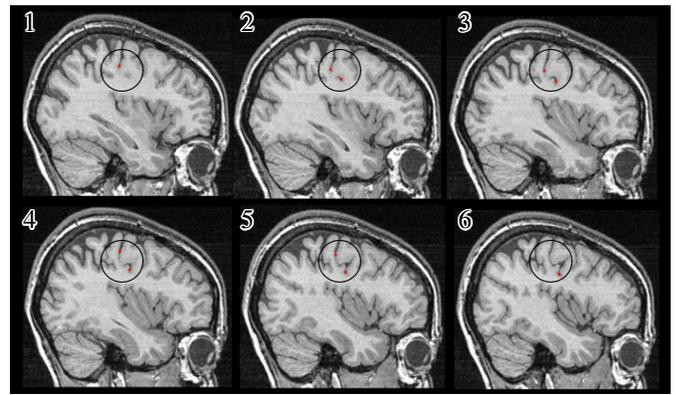

Fig. 14. Manual labeling of the central sulcus fundi in 6 consecutive slices of the original MRI volume: If the sulcus is parallel to the plane of section, manual-labeling may miss points in the areas indicated in Fig. 13.
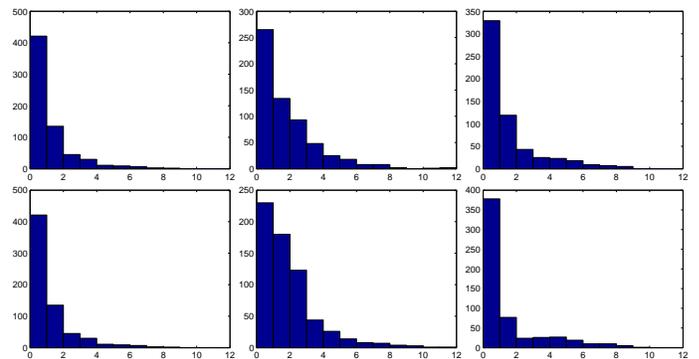

Fig. 15. The histograms of $r = \|p_s - p_a\|$ for three different brains. The horizontal axis is r and the vertical axis is the number of fundus points. The two rows show the results for the same brains for two different human raters.

labeled voxels p_m in each of the six brains, and the total percentages m_1, m_2 of points p_m for which $r < 2\ mm$ are given in the following table (the first two rows are rater 1, and the second two rows are rater 2; the columns correspond to the six different brains).

n_1	639	663	604	578	594	611
m_1	77%	83%	66%	77%	78%	70%
n_2	632	639	641	577	614	638
m_2	69%	62%	63%	79%	73%	73%

Following a careful examination of the automatic and manual labeling results, we can conclude that most of the errors arise for one of two reasons:

(1) An erroneous manually-labeled point. The sulcus penetrates deeply into the brain, and the fundus is difficult to visualize on the traditional three orthogonal planes. In Fig. 12 the automatically-labeled point, which lies on the fundus, is approximately $8\ mm$ away from the manually-labeled point, which lies above the fundus. Clearly our automatic algorithm outperforms the manually-labeled one in this case.

(2) The sulcus is extremely curvaceous, and the manually-labeled points are not contiguous because of the difficulty of identifying the sulcus on the three orthogonal planes. This is illustrated in Fig. 13, where we visually compare the automatically extracted fundi of two different central sulci to the manually obtained results by two different raters. If the sulcus is perpendicular to the plane of section, the manually-labeled points are quite accurate; however, if the sulcus is parallel to the plane of section (see Fig. 14), the manually-

labeled points may be far from each other in three dimensions. For the central sulci of Fig. 13 this is especially true for the curvaceous middle part which both raters miss consistently.

To give a more detailed analysis per major sulcal fundi we give the results of our comparison in the next table. The mean values per major sulci are taken over six brains for two different raters. We denote by $\bar{n}$ the mean of the number n of handmarked voxels per sulcal fundi, by $\bar{r}$ the mean of the distance value r, and by $\bar{m}$ the mean of the total percentage of voxels for which $r < 2\ mm$. Further, by $\sigma_{(\cdot)}$ we always denote the corresponding standard deviation.

	calc.	cent.	olfa.	prec.	supe.	temp.
$\bar{n}$	54.5	63.5	45.7	15.5	48.4	82.0
σ_n	4.2	3.8	4.3	4.0	10.9	10.0
$\bar{r}$	1.0	1.1	1.0	1.8	2.5	2.4
σ_r	0.4	0.4	0.4	0.9	0.8	0.6
$\bar{m}$	86%	86%	87%	63%	52%	55%
σ_m	9%	9%	9%	28%	19%	11%

The results suggest that it is more difficult to manually mark the precentral, superior frontal, and temporal sulcal fundi, than it is to manually label the calcarine, central, and olfactory sulcal fundi. Figure 16 shows overlaid axial projections for extracted fundi from six different brains as given by two raters
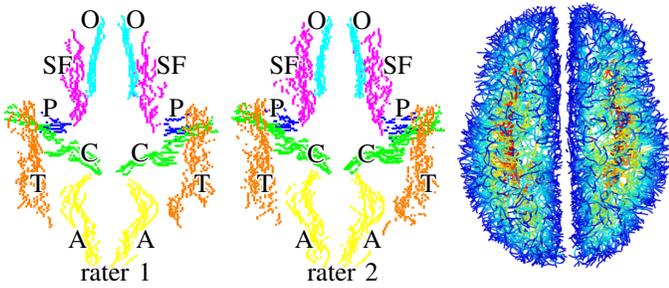
Fig. 16. (Left and middle) The 6 sulcal fundi manually-labeled by two expert anatomists overlaid for six different brains: calcarine A, central C, olfactory O, precentral P, superior frontal SF, temporal T. (Right) All automatically extracted fundi overlaid for six different brains.

Fig. 17. (Left) Distances $d_1, \ldots, d_4$ measured between fundal curves f_i and surfaces s_j for the reproducibility example (see text for details). (Right) All fundal curves f_1 and f_2 of the same hemisphere extracted using surfaces s_1 and s_2.

and our automated procedure. Note that the raters' explicit task was to label voxels corresponding to only six named sulci per hemisphere and this task required approximately 12 hours per brain volume, while our automated procedure returns spline curves for all locations that correspond to our geometric/algorithmic definition of sulcal fundi.

To conclude, our detailed examination of individual cases of high divergence between the automatically and manually labeled fundi, showed that these cases are generally due to either errors in the surface mesh extraction or errors in the manual labels, not in the automatic fundal extraction procedure we propose. The automatically extracted fundal curves are similar to the "gold-standard" fundal outlines defined manually by the anatomist. If the extracted pial surface is correct, then the automatic results look more accurate than the manually-labeled ones.

C. Reproducibility Evaluation of our Algorithm

The image volumes for the reproducibility experiment were rigidly aligned prior to surface extraction using the methods described in [26] so that the coordinates of their extracted surfaces and sulcal fundi would be directly comparable in a common Euclidean frame. For the result below we use an MPRAGE image from session 1 and an SPGR image from session 2. We name the extracted surfaces s_1 and s_2, and the automatic-labeled fundal curves f_1 and f_2 respectively. For each point p_1 on the fundal curve f_1, we look for the nearest point q_2 on the surface s_2 and the nearest point r_2 on the fundal curve f_2, and vice versa, see Fig. 17. We compute distances $d_1 = \|p_1 - q_2\|, d_2 = \|p_1 - r_2\|, d_3 = \|p_2 - q_1\|, d_4 = \|p_2 - r_1\|$ and differences $\delta_1 = |d_1 - d_2|, \delta_2 = |d_3 - d_4|$. The mean μ and standard deviation σ of d_i and δ_j are given in the table below:

	d_1	d_2	δ_1	d_3	d_4	δ_2
μ	0.405	0.913	0.508	0.464	0.959	0.495
σ	0.327	1.061	1.002	0.474	1.251	1.176

We see that corresponding fundal curves extracted on two different surfaces of the same brain are on average less than $1\ mm$ away from each other. The fundal curves on one surface are on average about $0.4\ mm$ away from the other surface. Thus we conclude that our algorithm gives promising results concerning reproducibility with an average deviation from the surface displacement of less than a pixel.
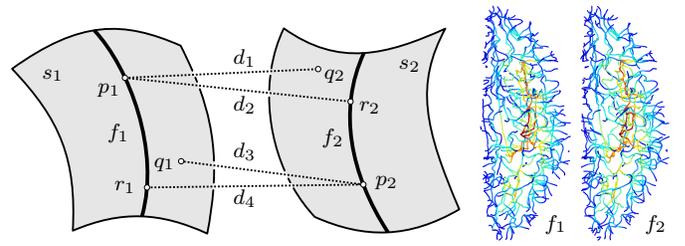
IV. RELATION TO PREVIOUS WORK

Previous work on automatic sulci extraction have made use of both voxel-based and surface mesh-based representations of cortical sulci. Voxel-based approaches possess a simplicity advantage by being closer to the image and its initial tissue-classified representations, but suffer the important representational disadvantage that a $1\ mm^3$ grid cannot simultaneously represent accurate cortical topology and pial surface location. This is because the CSF channels separating distinct, but spatially opposed gyri, are often an order of magnitude thinner than $1\ mm$. Other advantages of surface-based representations include their greater suitability for 3D visualization and the fact that they do not require an additional algorithmic stage to transform them to surface-based landmarks for surface-based warping applications. In contrast to the latter point, note that surface-based landmarks typically maintain their identity as coordinates within the image volume (i.e. they can still be used to guide volumetric warping).

Previous approaches to sulcal fundi extraction can be roughly divided into two distinct approaches: those based on *curvature* and those based on *distance functions*. Curvature based approaches define sulcal fundi as curves lying within areas of the extremal mean or principal surface curvature, whereas distance based approaches define them as curves whose distance to a hull bounding the cortical surface is locally maximal in the plane that is transverse to each given point on the curve.

Previous curvature based approaches are only semi-automatic: two or more end points of a sulcus are manually defined, and then a curve connecting these points lying within areas of extremal mean or principal surface curvature is computed. The proposed methods that follow this approach are, for example, dynamic programming [27], weighted geodesics computed by fast marching methods on triangular meshes [28], or fast marching methods on implicit surfaces [29]. Tracing in principal curvature directions has also been proposed in the volumetric setting [30] and in the parameter domain of a conformal parametrization [31].

Distance-based approaches often compute medial sulcal ribbons using the volumetric regions that result from subtracting WM, GM, and ventricular labeled voxels from the bounding hull volume. They define the fundi as the deepest boundaries of these surfaces [32], [20], or as the projection of these boundaries onto a triangle mesh representing the cortical

surface [33]. Previous work that combines curvature- and distance-based computations are semi-automatic algorithms that compute fundal curves using a modified fast-marching algorithm on triangular meshes [34] or on a flat map of the cortical surface [35].

Distance-based computations are generally more stable than curvature-based computations due to the perturbation damping properties of the L^2 distance norm and perturbation amplifying properties of differential operators typically used in computing curvature. Our method, based on distance computations, can be expected to yield robust results. This is of significant concern for this application domain because current technologies for surface mesh extraction necessarily operate on noisy, under-sampled MRI images of the geometrically convoluted human cortex, and as such are highly unstable [36].

V. CONCLUSIONS AND FUTURE RESEARCH

In this paper we proposed a geometric approach for the automatic extraction of sulcal fundi. This approach provides a novel definition of fundal depth and extracts the fundi as curves lying on a triangular-mesh representation of the pial surface. Extraction of the curves directly on the pial surface is useful for downstream applications that employ sulcal fundi as anatomic landmarks for surface-based intersubject registration. Our validation and reproducibility experiments demonstrate that the algorithm is robust, stable, and consistent with anatomical theory. Detailed examination of the results showed that errors in the extracted surfaces our algorithm takes as inputs probably account for large fractions of its error and variance. Because our fundal extraction algorithm can work with any closed mesh representing the cortical GM/CSF surface (modulo file format transformations), overall algorithm performance should benefit from future improvements in surface extraction algorithms and underlying MRI technology.

Another strategy of some interest is to produce fundus like landmarks on meshes representing the parallel GM/WM surface. While it is less appealing for anatomical visualization, the GM/WM surface has the advantage of being an easier target for automated surface extraction because its discrete voxel based topology is much less ambiguous. Results of a preliminary investigation into the applicability of our algorithm (with some modified parameter values) to estimation of fundal curves on the GM/WM surface are illustrated in Fig. 18. Preliminary analysis reveal strong parallelism between corresponding fundi from GM/WM and GM/CSF based surfaces.

Future research directions to be pursued include the examination of the utility of our extracted fundi and sulcal depth measurements for landmark and dense/iconic approaches to surface-based brain warping (of both GM/CSF and GM/WM surfaces) as well as algorithms for automatic naming/detection of cortical landmarks. Another important direction is to test the overall suitability of the algorithm, with possibly modified parameter values, for different types of brains (i.e. children and non-normals).

REFERENCES

[1] P. Kochunov, J.-F. Mangin, T. Coyle, J. Lancaster, P. Thompson, D. Rivière, Y. Cointepas, J. Régis, A. Schlosser, D. R. Royall, K. Zilles,
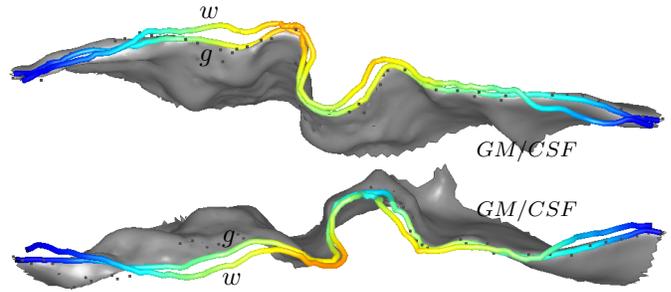

Fig. 18. For the central sulci of the same brain (left and right hemisphere) we show the fundal curves g extracted on the GM/CSF surface, and the fundal curves w extracted on the WM/GM surface (not shown). The fundal curves are shown as thick 3D curves and are 'parallel' to each other. The dots are manually traced fundal voxels and are shown for comparison.

J. Mazziotta, A. Toga, and P. T. Fox, "Age-related morphology trends of cortical sulci," *Human Brain Mapping*, vol. 26, no. 3, pp. 210–220, 2005.

[2] J. Régis, J.-F. Mangin, T. Ochiai, V. Frouin, D. Rivière, A. Cachia, M. Tamura, and Y. Samson, "Sulcal root generic model: a hypothesis to overcome the variability of the human cortex folding patterns," *Neurol Med Chir (Tokyo)*, vol. 45, pp. 1–17, 2005.

[3] P. Thompson and A. Toga, "A surface-based technique for warping 3-dimensional images of the brain," *IEEE TMI*, vol. 15, no. 4, pp. 402–417, 1996.

[4] J.Glaunes, M. Vaillant, and M. Miller, "Landmark matching via large deformation diffeomorphisms on the sphere," *Journal of Mathematical Imaging and Vision*, vol. 20, pp. 179–200, 2004.

[5] D. Collins, G. LeGoualher, and A. Evans, "Non-linear cerebral registration with sulcal constraints," in *First International Conference on Medical Image Computing and Computer-Assisted Intervention*, 1998, pp. 974–984.

[6] P. Hellier and C. Barillot, "Coupling dense and landmark-based approaches for nonrigid registration," *IEEE TMI*, pp. 217–227, 2003.

[7] M. Vaillant and C. Davatzikos, "Hierarchical matching of cortical features for deformable brain image registration," in *Lecture Notes in Computer Science: Information Processing in Medical Imaging '99*, vol. 1613, 1999, pp. 182–195.

[8] P. Thompson, K. Hayashi, E. Sowell, N. Gogtay, J. Giedd, J. Rapoport, G. de Zubicaray, A. Janke, S. Rose, J. Semple, D. Doddrell, Y. Wang, T. van Erp, T. Cannon, and A. Toga, "Mapping cortical change in Alzheimer's disease, brain development, and schizophrenia," *NeuroImage*, vol. 23, no. S1, pp. 2–18, 2004.

[9] A. Dale, B. Fischl, and M. Sereno, "Cortical surface-based analysis I. Segmentation and surface reconstruction," *NeuroImage*, vol. 9, pp. 179–194, 1999.

[10] J. Larsson, "Imaging vision: functional mapping of intermediate visual processes in man." PhD Thesis, Karolinska Institutet, Stockholm, Sweden, 2001, iSBN: 91-7349-090-3.

[11] J.-F. Mangin, D. Rivière, A. Cachia, E. Duchesnay, Y. Cointepas, D. Papadopoulos-Orfanos, P. Scifo, T. Ochiai, F. Brunelle, and J. Régis, "A framework to study the cortical folding patterns," *NeuroImage*, vol. 23, no. Supplement 1, pp. S129–S138, 2004.

[12] X. Han, D. Pham, D. Tosun, M. Rettmann, C. Xu, and J. Prince, "CRUISE: cortical reconstruction using implicit surface evolution," *NeuroImage*, vol. 23, pp. 997–1012, 2004.

[13] S. Smith, "Fast robust automated brain extraction," *Human Brain Mapping*, vol. 17, pp. 143–155, 2002.

[14] S. Mauch, "A fast algorithm for computing the closest point and distance transform," in *http://www.acm.caltech.edu/~seanm/projects/cpt/cpt.pdf*, 2000.

[15] C. Sigg, R. Peikert, and M. Gross, "Signed distance transform using graphics hardware," in *Proc. IEEE Visualization '03*, 2003, pp. 83–90.

[16] Y.-H. R. Tsai, L.-T. Cheng, S. Osher, and H.-K. Zhao, "Fast sweeping algorithms for a class of Hamilton-Jacobi equations," *SIAM J. Numerical Analysis*, vol. 41, no. 2, pp. 659–672, 2003.

[17] C.-Y. Kao, S. Osher, and Y.-H. Tsai, "Fast sweeping methods for static Hamilton-Jacobi equations," *SIAM J. Numerical Analysis*, vol. 42, pp. 2612–2632, 2005.

[18] H. Zhao, "Fast sweeping method for eikonal equations," *Mathematics of Computation*, vol. 74, pp. 603–627, 2005.

[19] S. Osher and J. A. Sethian, "Fronts propagating with curvature-dependent speed: Algorithms based on Hamilton-Jacobi formulations," *Journal of Computational Physics*, vol. 79, pp. 12–49, 1988.

[20] G. Lohmann, "Extracting line representations of sulcal and gyral patterns in MR images of the human brain," *IEEE TMI*, vol. 17, no. 6, pp. 1040–1048, 1998.

[21] M. Rettmann, X. Han, C. Xu, and J. Prince, "Sulcal segmentation using watersheds on the cortical surface," *NeuroImage*, vol. 15, pp. 329–344, 2002.

[22] A. Aho, J. Hopcroft, and J. Ullman, *Data Structures and Algorithms*. Addison-Wesley, Reading, Massachutes, 1983.

[23] D. Levin, "The approximation power of moving least-squares," *Math. Comput.*, vol. 224, no. 67, pp. 1517–1531, 1998.

[24] T. Cormen, C. Leiserson, R. Rivest, and C. Stein, *Introduction to Algorithms*. MIT Press, Massachusetts; McGraw-Hill, Boston, 2001.

[25] M. Hofer and H. Pottmann, "Energy-minimizing splines in manifolds," *ACM Trans. on Graphics*, vol. 23, no. 3, pp. 284–293, 2004.

[26] K. Clark, R. Woods, D. Rottenberg, A. Toga, and J. Mazziotta, "Impact of acquisition protocols and processing streams on tissue segmentation of t1 weighted mr images," *Neuroimage*, vol. 29, no. 1, pp. 185–202, 2006.

[27] N. Khaneja, M. Miller, and U. Grenander, "Dynamic programming generation of curves on brain surfaces," *IEEE PAMI*, vol. 20, pp. 1260–1265, 1998.

[28] A. Bartesaghi and G. Sapiro, "A system for the generation of curves on 3D brain images," *Human Brain Mapping*, vol. 14, pp. 1–15, 2001.

[29] F. Mémoli, G. Sapiro, and P. Thompson, "Implicit brain imaging," *NeuroImage*, vol. 23, no. S1, pp. 179–188, 2004.

[30] C. Renault, M. Desvignes, and M. Revenu, "3D curves tracking and its application to cortical sulci detection," *ICIP 2000*, vol. 2, pp. 491–494, 2000.

[31] L. M. Lui, Y. Wang, T. F. Chan, and P. M. Thompson, "Automatic landmark tracking applied to optimize brain conformal mapping," in *Proc. ISBI'06*. IEEE (electronic), 2006, pp. 205–208.

[32] G. L. Goualher, E. Procyk, D. Collins, R. Venugopal, C. Barillot, and A. Evans, "Automated extraction and variability analysis of sulcal neuroanatomy," *IEEE TMI*, vol. 18, no. 3, pp. 206–217, 1999.

[33] A. Cachia, J. Mangin, D. Rivière, F. Kherif, N. Boddaert, A. Andrade, D. Papadopoulos-Orfanos, J.-B. Poline, I. Bloch, M. Zilbovicius, P. Sonigo, F. Brunelle, and J. Régis, "A primal sketch of the cortex mean curvature: a morphogenesis based appraoch to study the variability of the folding patterns," *IEEE TMI*, vol. 22, no. 6, pp. 754–765, 2003.

[34] X. Tao, X. Han, M. Rettmann, J. Prince, and C. Davatzikos, "Statistical study on cortical sulci of human brains," in *Proc. IPMI'01*, vol. LNCS 2082, 2001, pp. 475–487.

[35] X. Tao, J. Prince, and C. Davatzikos, "An automated method for finding curves of sulcal fundi on human cortical surfaces." in *ISBI*, 2004, pp. 1271–1274.

[36] T. Jarvis, K. Schaper, K. Rehm, and D. Rottenberg, "Quantitative evaluation of surface extraction reproducibility," in *Neuroimage 26 CD-ROM Abstract #760*, 2005.

Guillermo Sapiro (M'95) received his Ph.D. from The Technion-Israel Institute of Technology in 1993. He is currently with the Department of Electrical and Computer Engineering at the University of Minnesota, where he holds the position of Distinguished McKnight University Professor. He works on differential geometry and geometric partial differential equations, both in theory and applications in computer vision, computer graphics, medical imaging, and image analysis. He has authored and co-authored numerous papers in this area and has written the book "Geometric Partial Differential Equations and Image Analysis" published by Cambridge University Press, January 2001.

Josh Stern received a B.A. and B.S.E. from the University of Pennsylvania and a Ph.D. from M.I.T. He is currently Assistant Professor of Neurology at the University of Minnesota doing research on automated methods of analyzing structural and functional MRI.

Kelly Rehm received a Ph.D. in Optical Sciences from the University of Arizona (1992). She is currently an Assistant Professor in the Department of Radiology at the University of Minnesota. Through her work with the International Neuroimaging Consortium she specializes in brain mapping methodologies.

Chiu-Yen Kao received her Ph.D. in Mathematics from the University of California, Los Angeles. Currently she is an Industrial Postdoc at the Institute for Mathematics and its Applications in Minneapolis. Her research expertise lies in level set methods, Hamilton-Jacobi equations, computational anatomy, and inverse problems.

David A. Rottenberg M.Sc. (Cantab), M.D., Professor of Neurology and Radiology at the University of Minnesota, directs the International Neuroimaging Consortium (http://neurovia.umn.edu/INC), which consists of six North American and four foreign research institutions and has been continuously funded by the Human Brain Project since 1994. Dr. Rottenberg's research interests include computational anatomy and scientific visualization, and he has authored and co-authored numerous publications relating to PET, MRI, and fMRI.

Michael Hofer received his Ph.D. in Mathematics from Vienna University of Technology (2005). Following his Ph.D. studies he was a Postdoc at the University of Minnesota and is now a Postdoc at the Geometric Modeling and Industrial Geometry research group in Vienna. His research focuses on application oriented fundamental research in geometry, geometric modeling and processing, and imaging sciences.